Electronic Supplementary Information

Control over Interpenetration for Boosting Methane Storage Capacity in Metal–Organic Frameworks

Jing Tan,[‡a] Yu Tao,[‡a] Xiangyu Zhang,[‡a] Qing Wang,[a] Tengwu Zeng,[a] Zhaolin Shi,[a]

Kyle E. Cordova,[b] Yongjin Lee,*[a,c] Haiming Liu,*[a] and Yue-Biao Zhang*[a]

[a.] *School of Physical Science and Technology, ShanghaiTech University, Shanghai 201210, China.*

[b.] *Materials Discovery Research Unit, Advanced Research Centre, Royal Scientific Society (RSS), 11941 Amman, Jordan.*

[c.] *Department of Chemical Engineering, Inha University, Incheon 22212, Republic of Korea.201210, China.*

[†]These authors contributed equally.

*To whom correspondence should be addressed.

E-mail: leeyj@shanghaitech.edu.cn

or liuhm@shanghaitech.edu.cn

or zhangyb@shanghaitech.edu.cn

Table of Contents

Section S1. Syntheses and Characterization.....S3

Section S2. X-ray Diffraction Structure Analyses S11

Section S3. Porosity and Surface Area Analyses S17

Section S4. Methane Adsorption Measurements.....S29

Section S5. Solid-State NMR Spectroscopy S36

Section S6. Molecular Simulation.....S47

References.....S50

Section S1. Syntheses and Characterization

Materials and Instrumentation. All of the chemicals were purchased from commercial sources and used as received without further purification unless otherwise stated. $Zn(NO_3)_2 \cdot 6H_2O$, diethylformamide (DEF), ethanol, and methanol were obtained from the Shanghai Aladdin Bio-Chem Technology Co, LTD, and 4,4′,4″-nitrilotrisbenzoic acid (H_3NTB) was obtained from the Chemsoon Co. Ltd.

Elemental analyses (EA) were carried out on a PerkinElmer 2400 Series II CHN elemental analyser. PXRD patterns were collected on a Bruker D8 ADVANCE X-ray diffractometer using Cu Kα radiation (λ = 1.54184 Å). NMR spectrum was recorded on a Bruker AVANCE III HD 500 MHz NMR spectrometer. The thermal gravimetric analyses (TGA) were carried out using a PerkinElmer Q50 TGA analyser from 25 to 700 °C under N_2 atmosphere with temperature ramping rate of 5 °C/min. The Fourier-transform infrared (FT-IR) spectra were recorded on neat samples in the range of 4,000–500 cm^{-1} on a PerkinElmer FT-IR Spectrometer equipped with single reflection diamond ATR module.

Synthesis of MOF-150, $Zn_4O(NTB)_2$: A mixture of $Zn(NO_3)_2 \cdot 6H_2O$ (11 mg, 0.038 mmol), H_3NTB (7.2 mg, 0.019 mmol) was dissolved in 4 mL of dimethylformamide (DEF) and ethanol mixed solvent (*v*/*v* = 7:3) in a 20 mL vial, and then the reaction mixture was sonicated for 10 minutes and placed in an oven at 85 °C for 48 hours, which is slightly different from synthetic methods previously reported in the literatures. After cooling to room temperature, the light brown crystals of MOF-150 were obtained with a yield of 46% based on NTB. If the ethanol changes into H2O, MOF-150 also was synthesized. EA of the sample for **$Zn_4O(NTB)_2$** ($C_{42}H_{24}N_2O_{13}Zn_4$): Calc.: C, 49.15; H, 2.35; N, 2.73%. Found: C, 47.63; H, 2.65; N, 2.91%. FT-IR (4000~500 cm^{-1}): 1587(m), 1535(s), 1505(s), 1385(m), 1312(s), 1272(s), 1175(s), 1145(s), 1105(s), 1013(s), 966(s), 925(s), 842(s), 778(m), 712(s), 700(s), 675(s), 628(s), 516(s).

Synthesis of ST-150, $Zn_4O(NTB)_2$: A mixture of $Zn(NO_3)_2 \cdot 6H_2O$ (12 mg, 0.04 mmol), 4,4',4"-nitrilotrisbenzoic acid (H_3NTB) (7.5 mg, 0.02 mmol) was dissolved in 4 mL of diethylformamide (DEF) solvent in a 20 mL vial, and then the reaction mixture was sonicated for 10 minutes and placed in an oven at 85 ºC for 48 hours. After cooling to room temperature, the colourless crystals of ST-150 were obtained with a yield of 46% based on H_3NTB. EA of the sample for **$Zn_4O(NTB)_2$** ($C_{42}H_{24}N_2O_{13}Zn_4$): Calc.: C, 49.15; H, 2.35; N, 2.73%. Found: C, 47.76; H, 3.60; N, 2.91%. FT-IR (4000~500 cm^{-1}): 1590(m), 1532(s), 1502(s), 1388(m), 1310(s), 1270(s), 1178(s), 1147(s), 1106(s), 1015(s), 969(s), 924(s), 844(s), 778(m), 710(s), 703(s), 675(s), 629(s), 518(s).

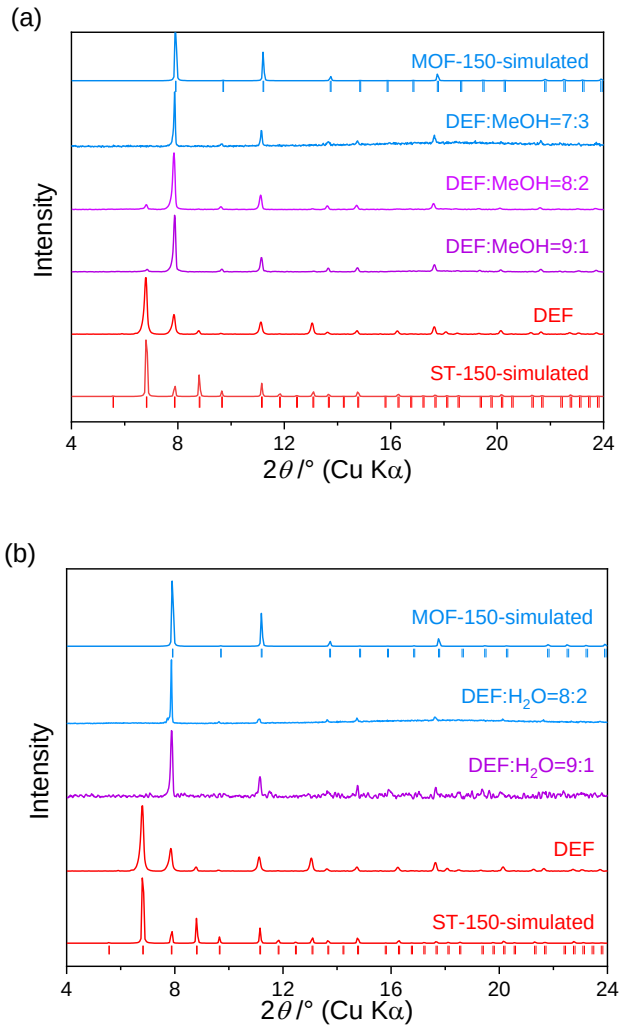

Figure S1 PXRD patterns of the products with various ratios of DEF and (a) MeOH, and (b) H_2O to show the solvent-directed syntheses.

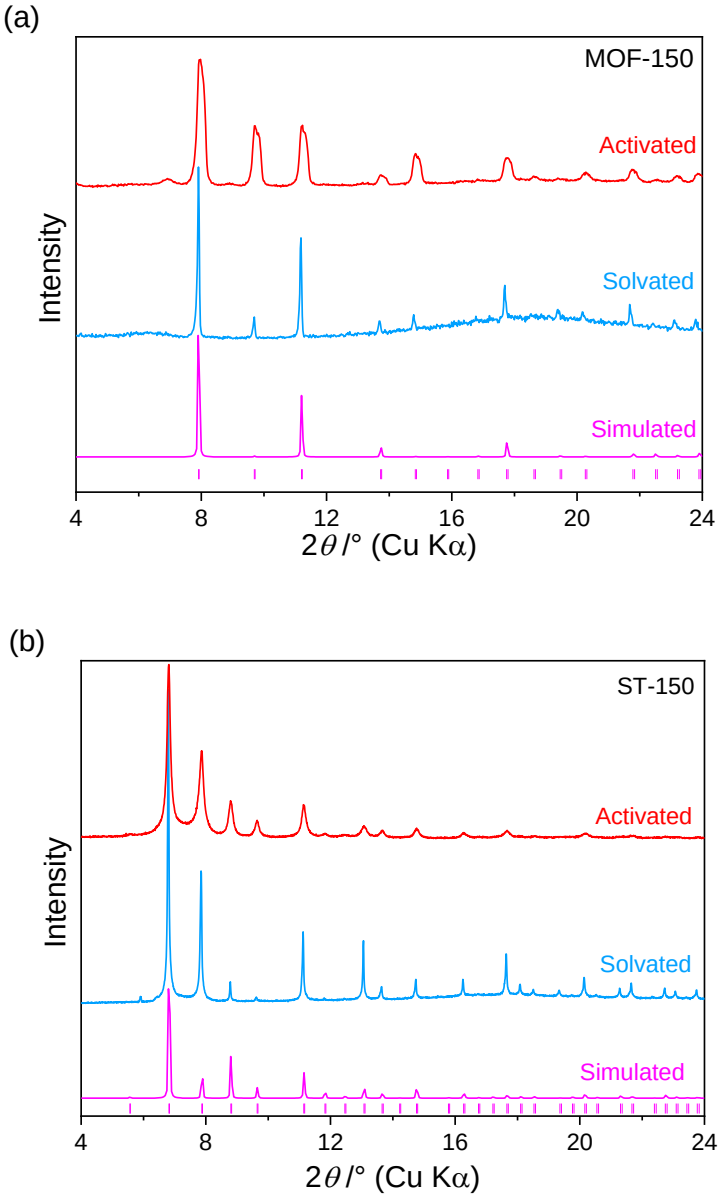

Figure S2. (a) The activated (red), solvated (blue), and simulated (magenta) PXRD patterns of MOF-150; (b) activated (red), solvated (blue), and simulated (magenta) PXRD patterns of ST-150.

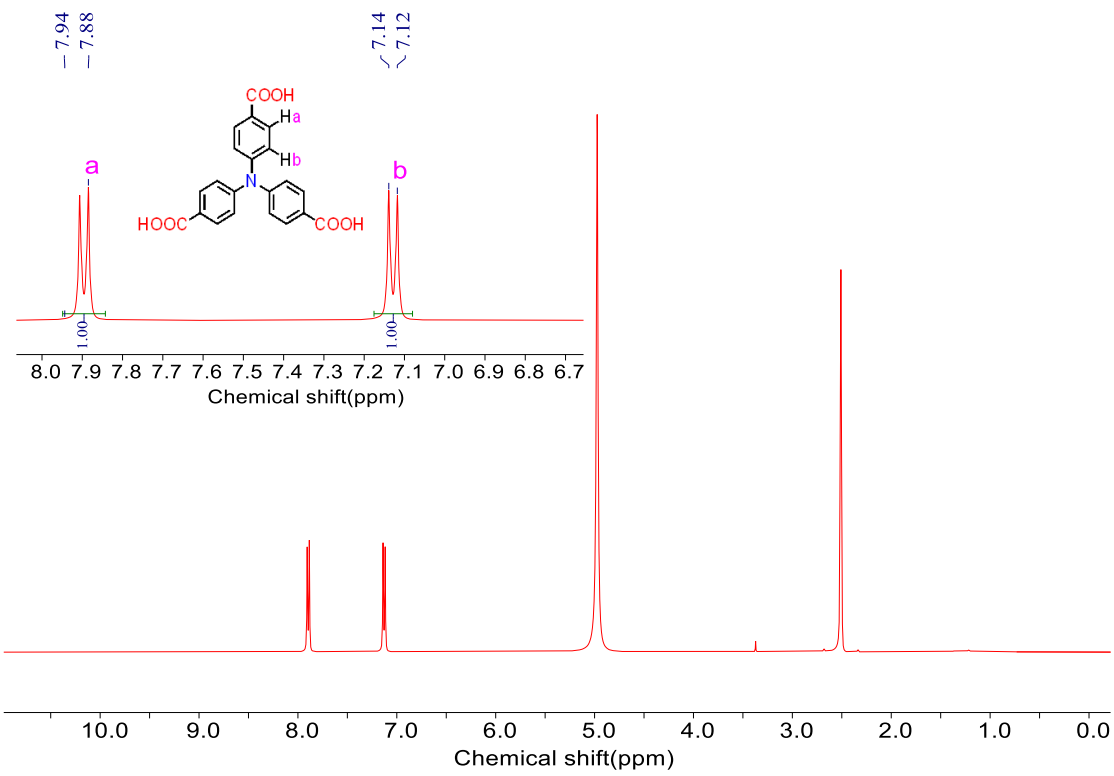

Figure S3. ^{1}H NMR spectrum of ST-150 digested in DMSO-d_6 with 20% DCl. The result shows the fully activation by the elimination of signal for guest molecules such as DEF, DMF, acetone, with only solvent peaks for DMSO and water.

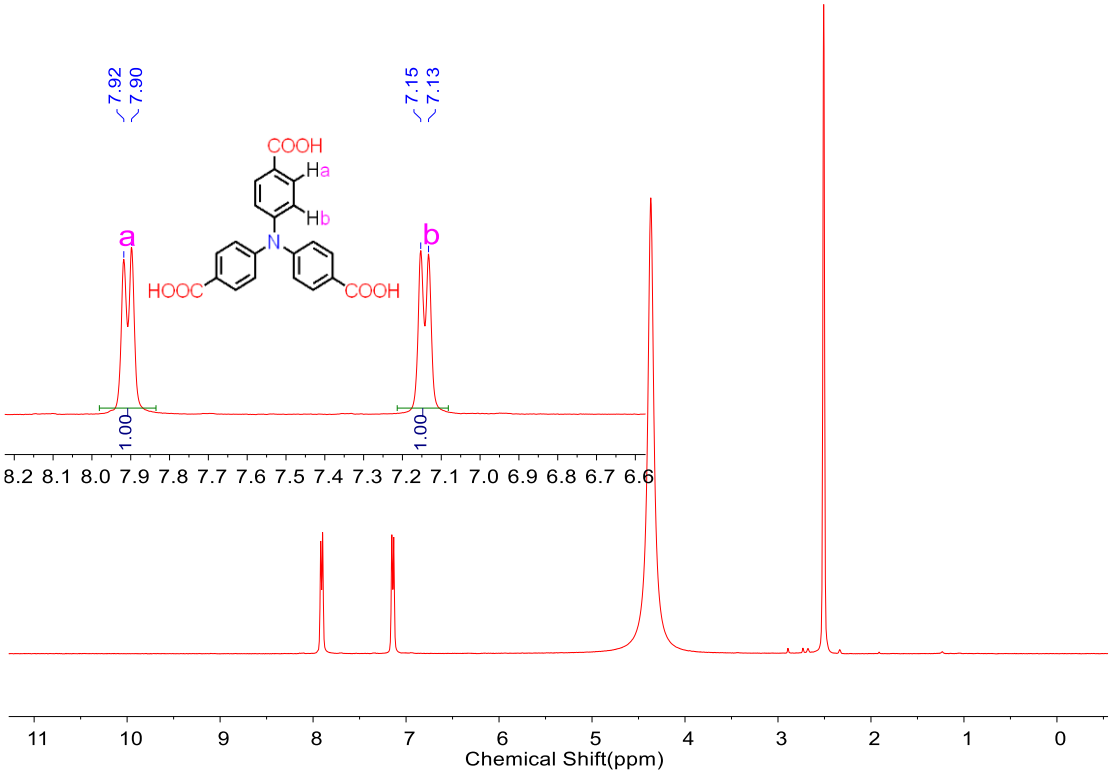

Figure S4. ^{1}H NMR spectrum of MOF-150 digested in DMSO-d_6 with 20% DCl. The result shows the fully activation by the elimination of signal for guest molecules such as DEF, DMF, acetone, with only solvent peaks for DMSO and water.

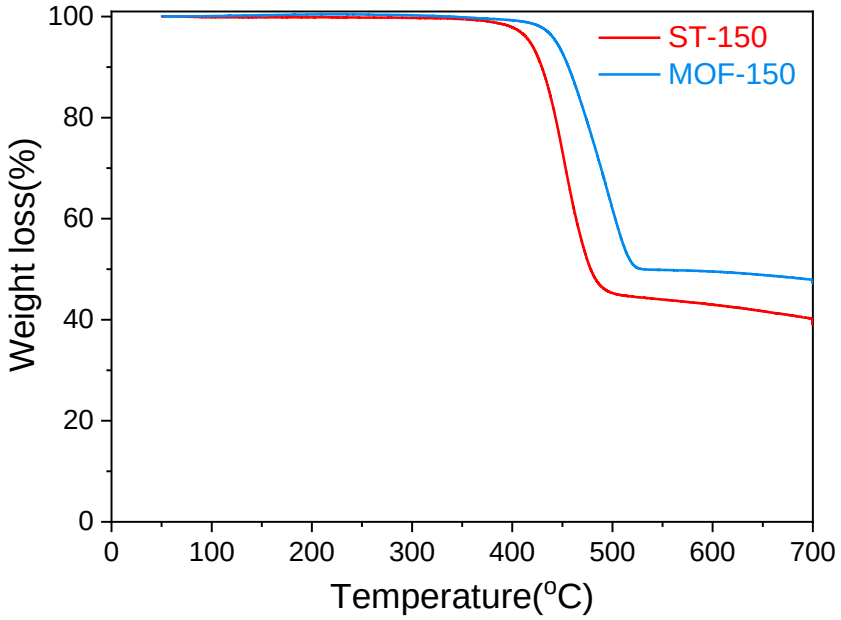

Figure S5. TG curves of for the activated sample of ST-150, MOF-150 under N_2 atmosphere. High thermal stability is indicated up to 450 °C under N_2. the weight almost unchanged before 400 °C for that of the ST-150 and MOF-150 can indicate no solvent molecules in the pore. And the weight loss before 200 °C for that of the ST-156 can be attributed to DMF in the pore.

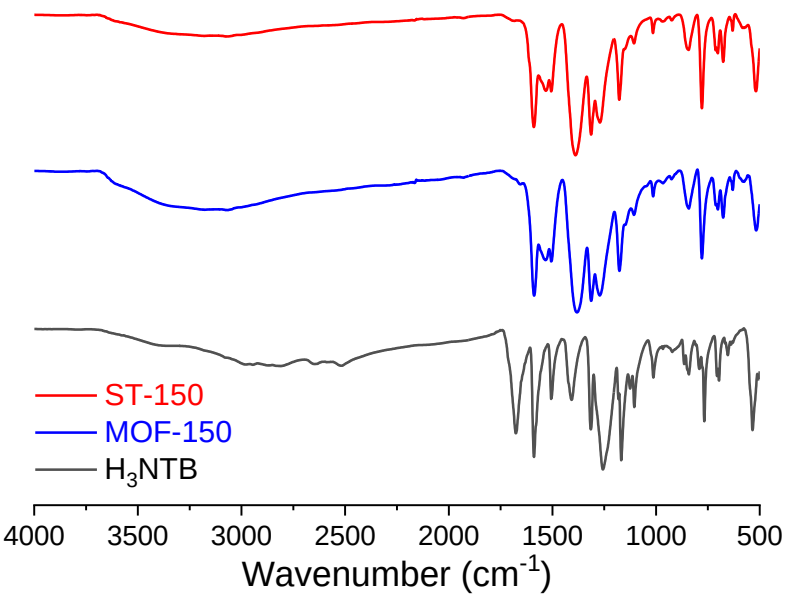

Figure S6. IR curves of (a) ST-150, (b) MOF-150, (c)the ligand of H_3NTB. The bands at 1600,1580,1500 and 1450 cm^{-1} characterize for the benzene ring. The -C-O- stretching vibration at 1275 and 1020 cm^{-1} indicates carboxyl. The three compounds have the same characteristic, indicating the same link and no solvent molecules.

Section S2. X-ray Diffraction Structure Analyses

Powder X-ray diffraction. High-resolution powder X-ray diffraction (PXRD) patterns were measured at the beamline BL14B1 of the Shanghai Synchrotron Radiation Facility (SSRF) using synchrotron radiation with a wavelength of 0.6895 Å and the transition optical mode. And the samples were heated in a glass capillary under vacuum before testing.

The structure models were built by using the Crystal Building module using the space groups and unit-cell parameters obtained from the Pawley refinements, and then optimized by the Forcite module using the universal force field. Rietveld refinements were performed to the modelled structures, in which the peak profiles, zero-shift, background, and unit-cell parameters, Berar–Baldinozzi asymmetry correction parameters, preferred orientation and global isotropic temperature factors were optimized step by step to meet good agreement between the calculated and the experimental powder diffraction patterns.

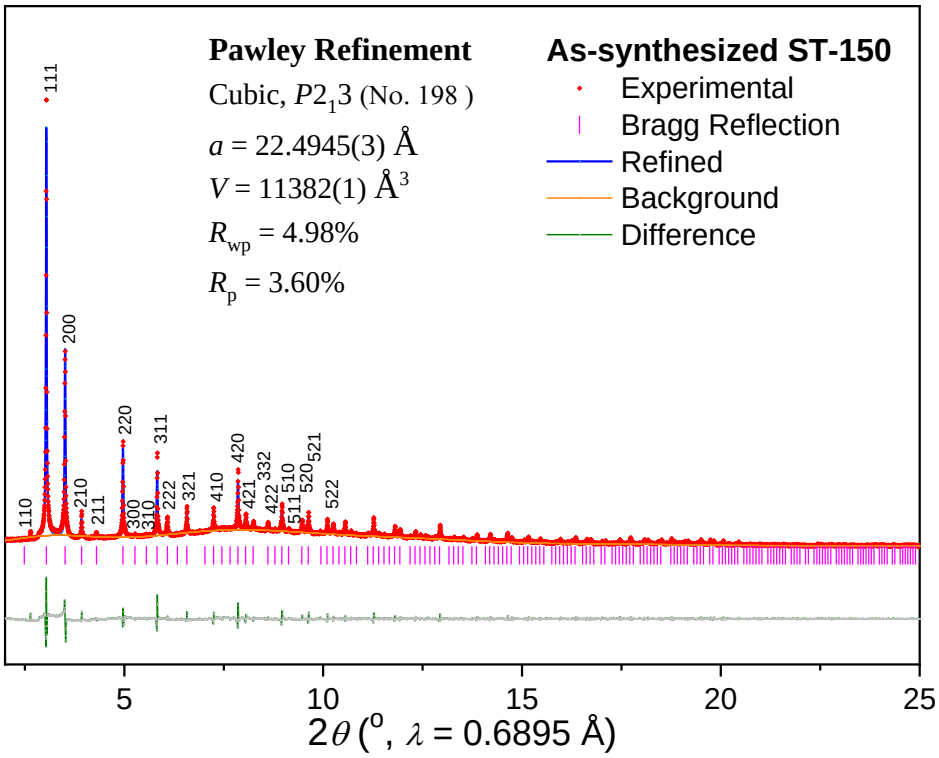

Figure S7. The synchrotron PXRD patterns of the as-synthesized ST-150 fitted by the Pawley refinement.

Table S1. Crystal data and Structure Refinements Results.

Compound	**ST-150**
Formula	$C_{42}H_{24}N_2O_{13}Zn_4$
Formula weight	1026.20
Crystal system	cubic
Space group	$P2_13$(No.198)
Z	4
Density(g/cm^3)	0.603
a (Å)	22.440(2)
V (Å^3)	11300(1)
R_p (%)	5.79 %
R_{wp} (%)	7.92 %

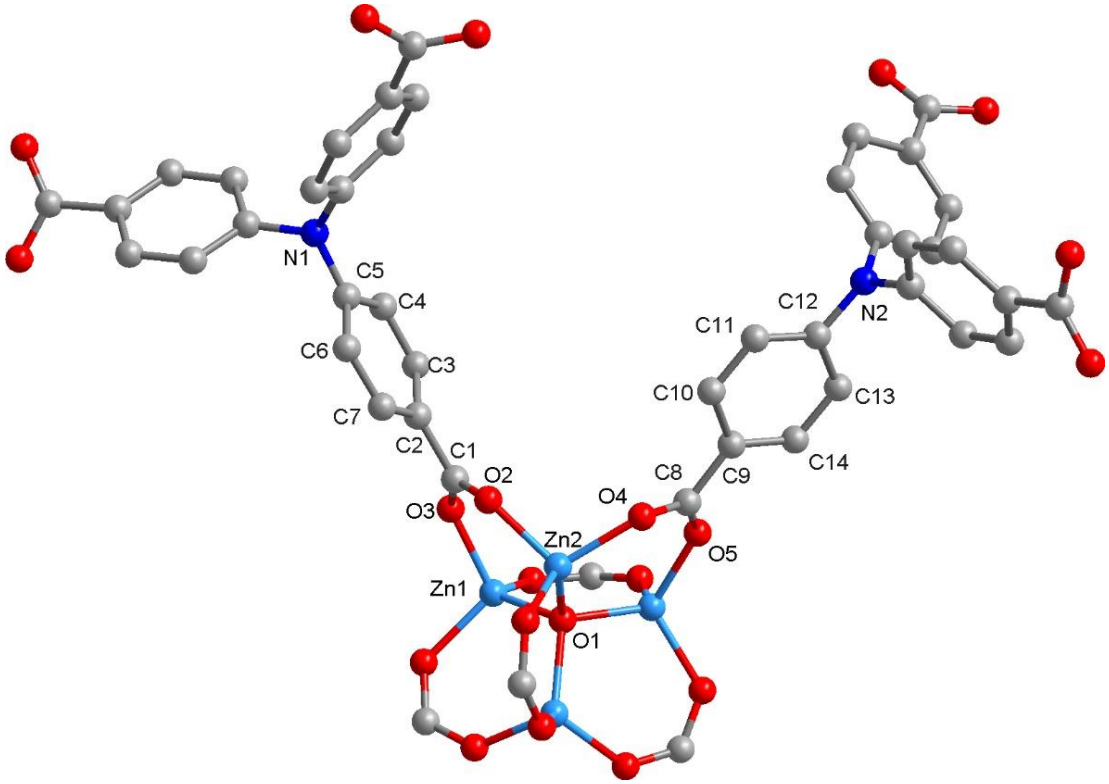

Figure S8. Asymmetric unit in the crystal structure of ST-150 (carbon, grey; nitrogen, blue; oxygen, red; zinc, light-blue). Hydrogen atoms are omitted for clarity; symmetry-related atoms are not labelled.

Table S2. Fraction Atomic Coordinates of ST-150.

Atom	***x***	***y***	***z***	**Atom**	***x***	***y***	***z***
Zn1	0.80046	0.19954	0.69954	O1	0.75023	0.24977	0.74977
Zn2	0.77655	0.3322	0.74866	O2	0.8481	0.3354	0.702
C1	0.8834	0.2974	0.681	O3	0.8728	0.2428	0.6762
C2	0.9406	0.3218	0.6596	O4	0.79728	0.36108	0.82781
C3	0.99421	0.29526	0.67059	O5	0.79474	0.27857	0.88155
C4	1.04601	0.32022	0.65195	N1	1.1012	0.3988	0.6012
C5	1.04586	0.37284	0.61826	N2	0.94253	0.44253	1.05747
C6	0.99180	0.39927	0.60581	H3	0.99524	0.25936	0.69126
C7	0.93983	0.37516	0.62617	H4	1.08205	0.30222	0.66163
C8	0.80982	0.33146	0.87308	H6	0.99075	0.43400	0.58323
C9	0.8451	0.35971	0.91984	H7	0.90378	0.39390	0.61802
C10	0.88232	0.40981	0.90778	H10	0.88541	0.42428	0.86908
C11	0.91348	0.43671	0.95270	H11	0.93688	0.46987	0.94433
C12	0.91073	0.41574	0.00917	H13	0.87130	0.35302	1.06170
C13	0.87429	0.36678	1.02273	H14	0.82011	0.30639	0.98694
C14	0.84325	0.33957	0.97797				

Single-crystal X-ray Diffraction. Single-crystal X-ray diffraction data were collected on a Bruker D8 Venture CCD diffractometer. Multi-scan absorption corrections were performed with Bruker APEX III. The structure model was solved by direct methods, and all non-H atoms were refined anisotropically with SHELXTL-2014 software package. All hydrogen atom positions were added by geometry and refined by a riding model.

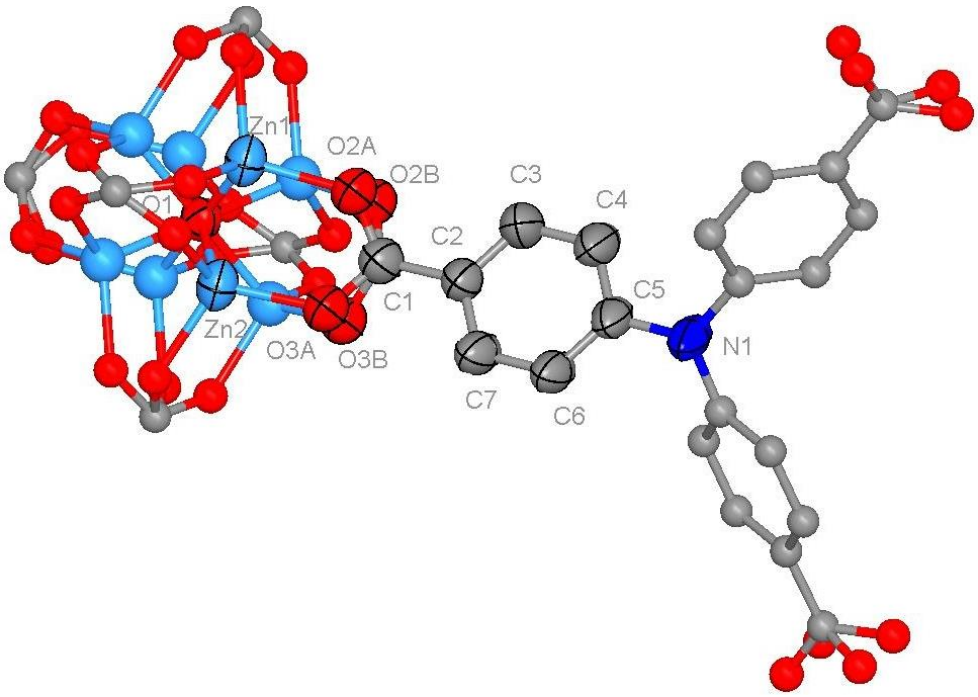

Figure S9. Asymmetric unit in the single crystal structure of MOF-150 (thermal ellipsoids with 50% probability; carbon, grey; nitrogen, blue; oxygen, red; zinc, light-blue). Hydrogen atoms are omitted for clarity; symmetry-related atoms are not labelled and represented as spheres.

Table S3. Crystallographic data and structure determination for MOF-150 (pyr)

Compound	**MOF-150**
Formula	$C_{42}H_{24}N_2O_{13}Zn_4$
Formula weight	1026.11
Crystal system	cubic
Space group	$Ia\bar{3}$ (*No.*176)
a (Å)	22.329(3)
V (Å^3)	11133(4)
Z	8
ρ (g cm^{-3})	1.224
Void fraction (%)	46.2
Crystal size (mm^3)	0.3 × 0.2 × 0.15
T (K)	298
λ (Å)	0.8265
θ range (°)	2.598–28.530
Unique reflections	1489
Resolution (Å)	0.87
Parameters	85
Restraints	102
R_1, wR_2	0.1523, 0.4577
Max./Min. 1e/Å^3)	2.02/-4.12

$^aR_1 = \Sigma||F_o| - |F_c||/\Sigma|F_o|$; $^bwR_2 = [\Sigma w(F_o^2 - F_c^2)^2/\Sigma w(F_o^2)^2]^{1/2}$; $^cS = [\Sigma w(F_o^2 - F_c^2)^2/(N_{ref} - N_{par})]^{1/2}$.

Table S4. Fractional Atomic Coordinates (×10^4) and Equivalent Isotropic Displacement Parameters (Å^2×10^3) for MOF-150. U_{eq} is defined as 1/3 of of the trace of the orthogonalized U_{ij} tensor.

Atom	*x*	*y*	*z*	$U_{eq.}$
Zn1	2980.0(9)	7980.0(9)	7020.0(9)	68.1(11)
Zn2	3247.2(8)	7650.3(8)	7906.8(9)	68.1(11)
O1	2500	7500	7500	60(3)
O2A	3625(7)	7491(8)	6700(7)	74.4(17)
O2B	3482(3)	7108(4)	6621(4)	74.4(17)
O3A	3885(4)	7199(4)	7545(4)	74.4(17)
O3B	3748(6)	6832(8)	7486(7)	74.4(17)
C1	3912(4)	7078(4)	6980(3)	76(2)
C2	4484.1(19)	6827(3)	6737(2)	69(2)
C3	4573(2)	6771(3)	6123.5(18)	91(3)
C4	5105(3)	6532(3)	5906.4(16)	98(3)
C5	5548(2)	6349(3)	6303(2)	79(2)
C6	5460(2)	6405(3)	6917(2)	83(3)
C7	4928(2)	6644(3)	7133.6(15)	82(3)
N1	6078(5)	6078(5)	6078(5)	96(4)

Section S3. Porosity and Surface Area Analyses

Activation Protocol of the MOF Materials. As-synthesized samples were further immersed in anhydrous CH_2Cl_2 with refresh solvent until the elimination of DMF in MOF monitored by NMR spectroscopy of digested solutions. The dried sample was quickly transferred to a sorption cell in a glovebox, which was further evacuated and heated at 100 °C overnight on a FLOVAC activation station from Quantachrome.

Specific Surface Area Analyses. The Brunauer-Emmett-Teller (BET) surface areas are all assessed from their N_2 physisorption isotherms according to the consistency criteria.[S1, S2]

Pore Size Distribution Analyses. The pore volumes were all estimated by the N_2 uptake plateau; the pore size distributions were all derived from their Ar physisorption isotherms at 87 K fitted by DFT method.[S3]

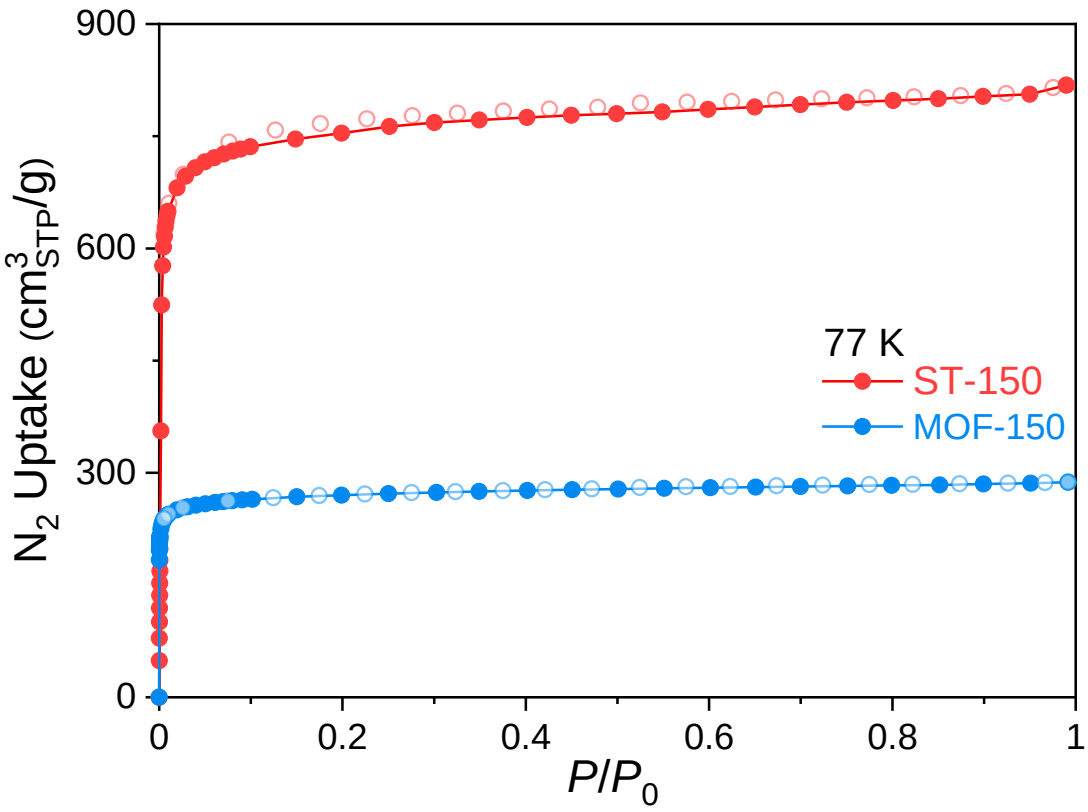

Figure S10. N_2 physisorption isotherms at 77 K for MOF-150 and ST-150 prepared in this work.

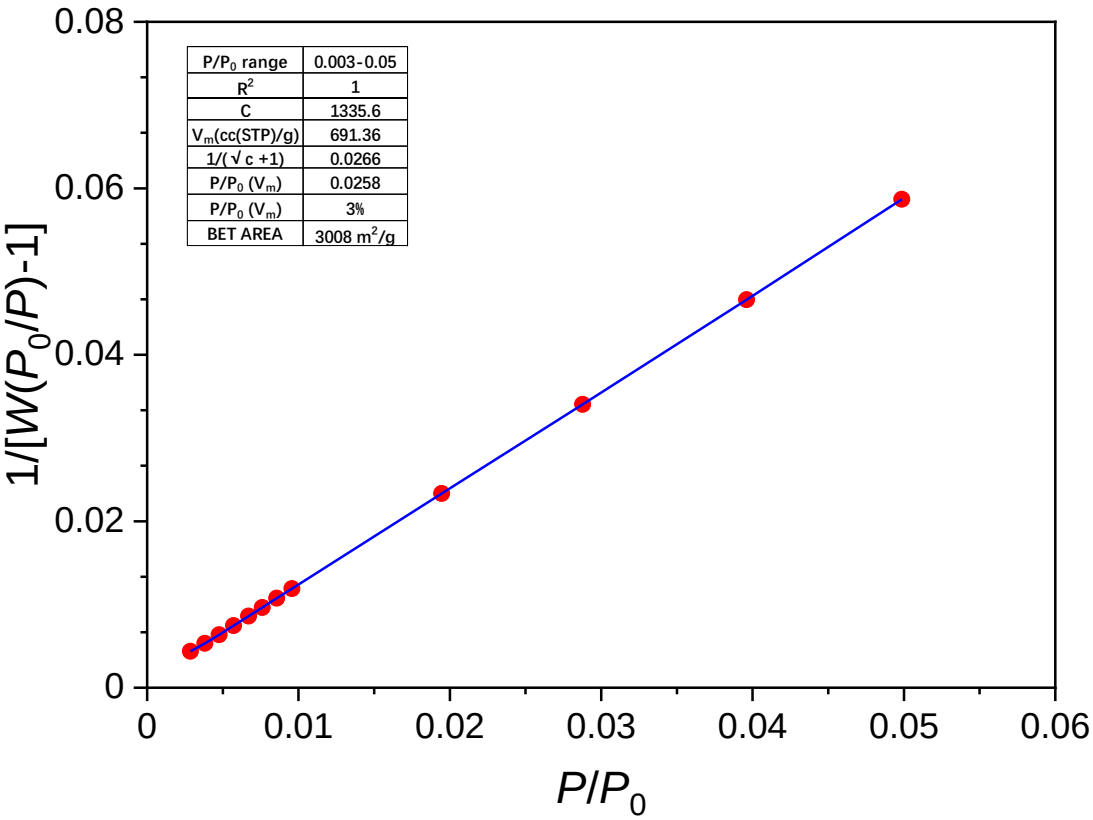

Figure S11. Multiple point BET plot of the N_2 adsorption isotherm for ST-150 gives a specific surface area of 3008 m^2/g. The table contains all the information relevant to the BET consistency criteria: P/P_0 range is selected based on the first consistency criterion; (1/(√C+1)) corresponds to the pressure of monolayer completion from BET-calculated, *V*m is the monolayer loading to calculate the BET surface area, the difference between (1/(√C+1)) and pressure of monolayer completion is less than 20%.

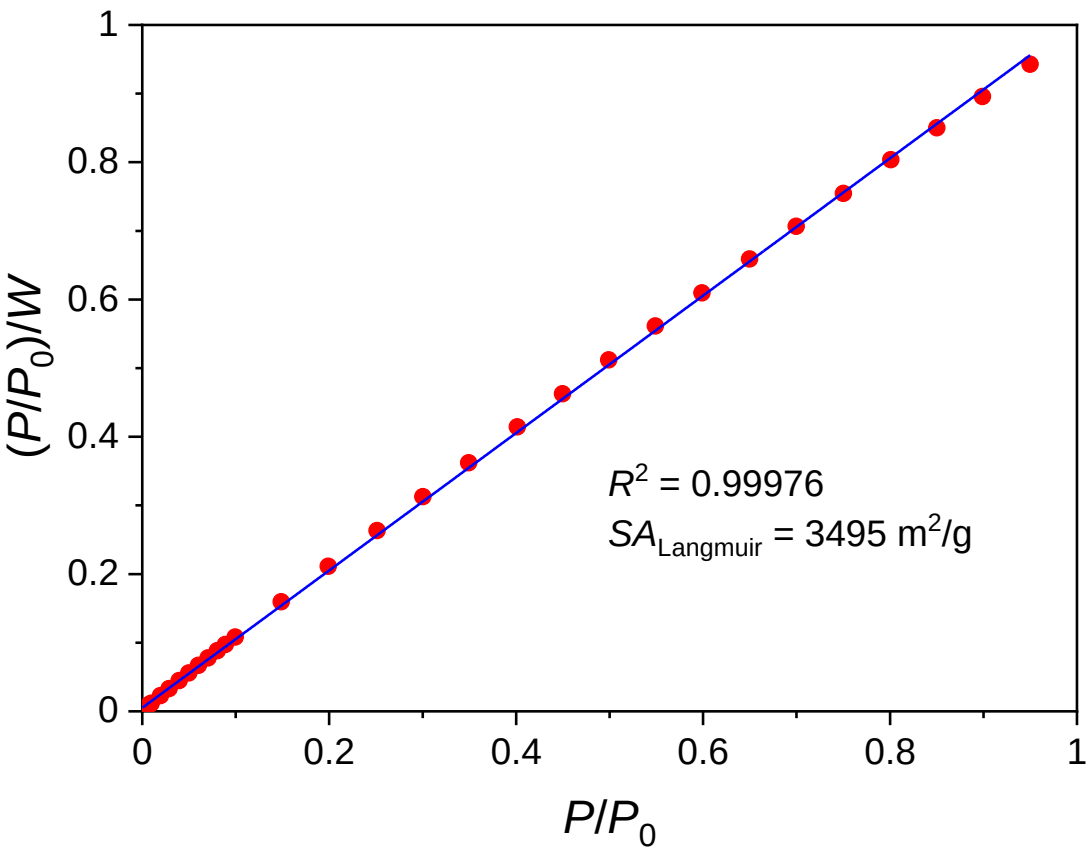

Figure S12. Langmuir plot of the N_2 adsorption isotherm for ST-150 giving a specific surface area of 3495 m^2/g.

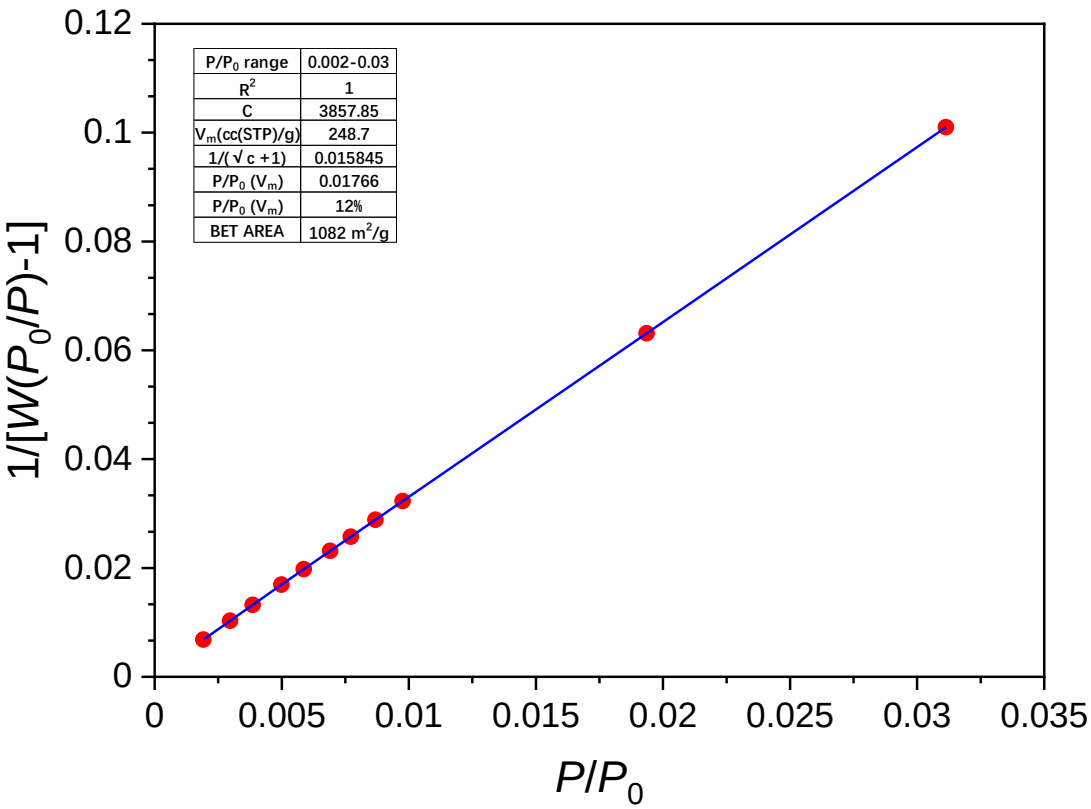

Figure S13. Multiple point BET plot of the N_2 adsorption isotherm for MOF-150 gives a specific surface area of 1082 m^2/g. The table contains all the information relevant to the BET consistency criteria: P/P_0 range is selected based on the first consistency criterion; (1/(√C+1)) corresponds to the pressure of monolayer completion from BET-calculated, V_m is the monolayer loading to calculate the BET surface area, the difference between (1/(√C+1)) and pressure of monolayer completion is less than 20%.

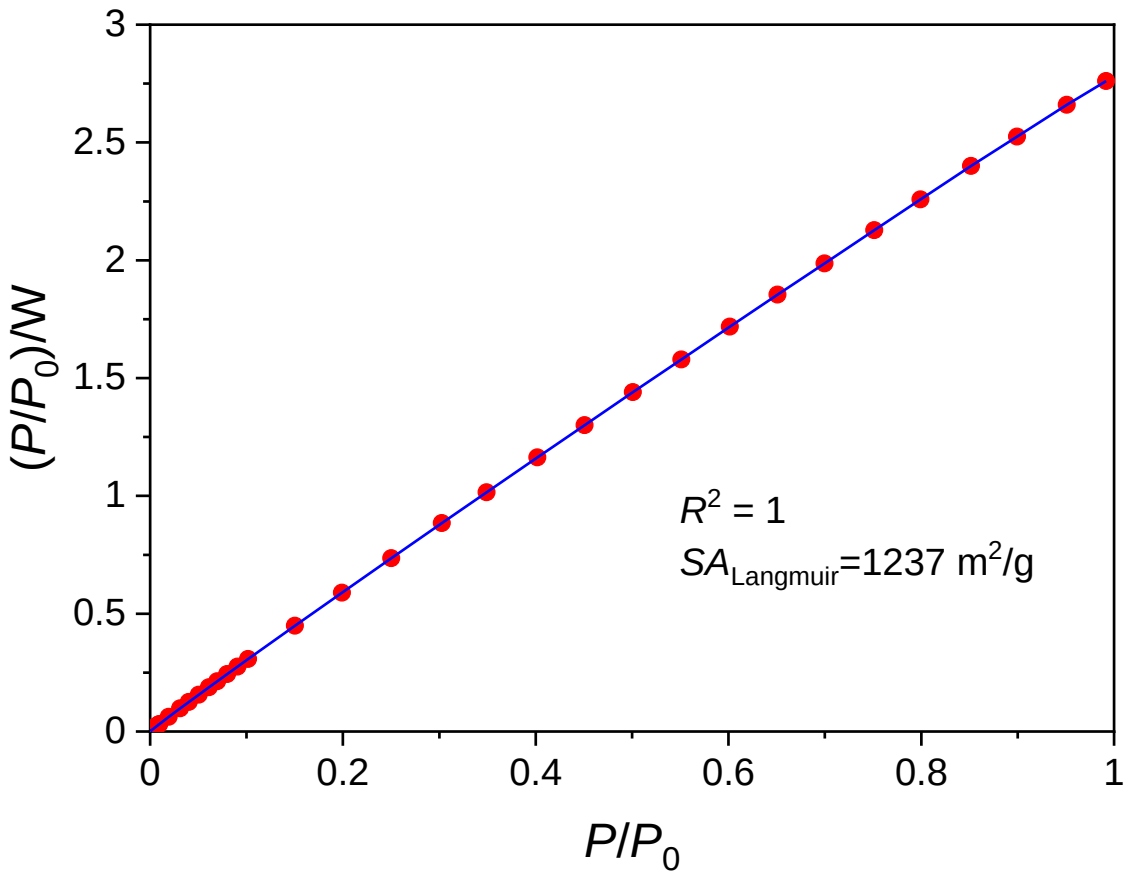

Figure S14. Langmuir plot of the N_2 adsorption isotherm for MOF-150 giving a specific surface area of 1237 m^2/g.

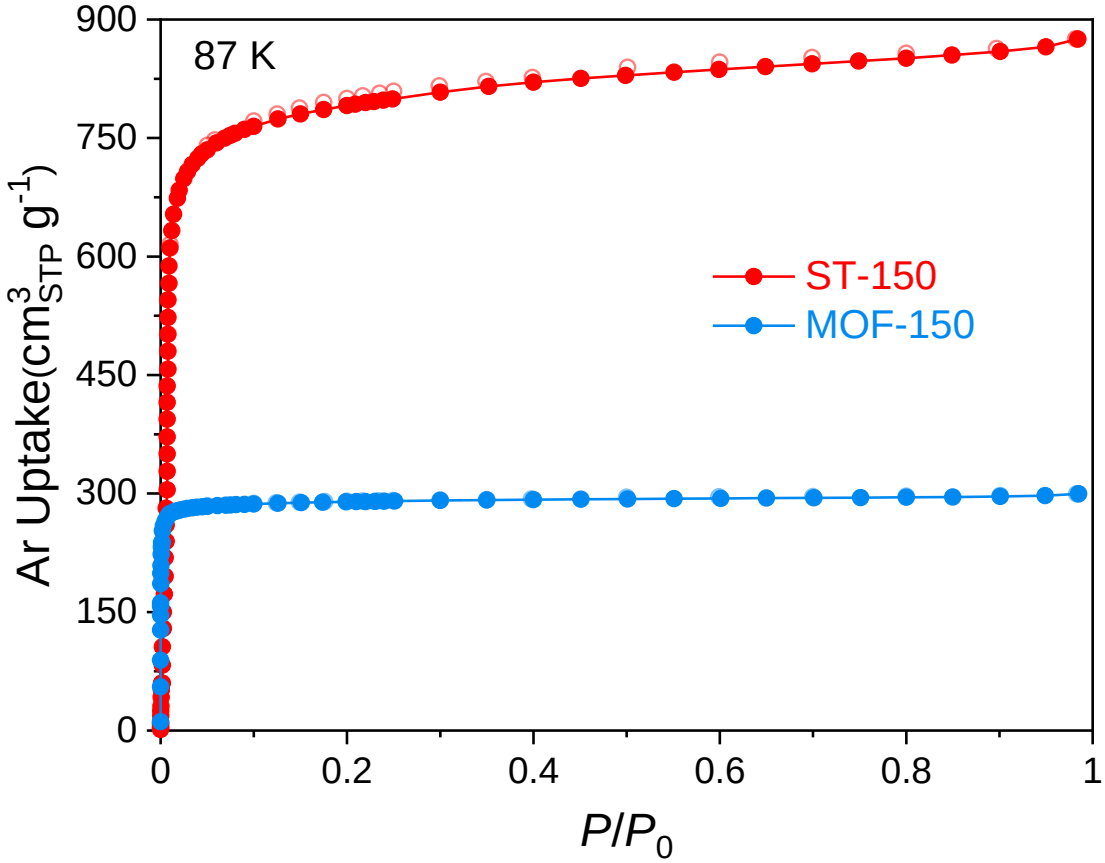

Figure S15. Ar physisorption isotherms at 87 K between ST-150 and MOF-150 prepared in this work.

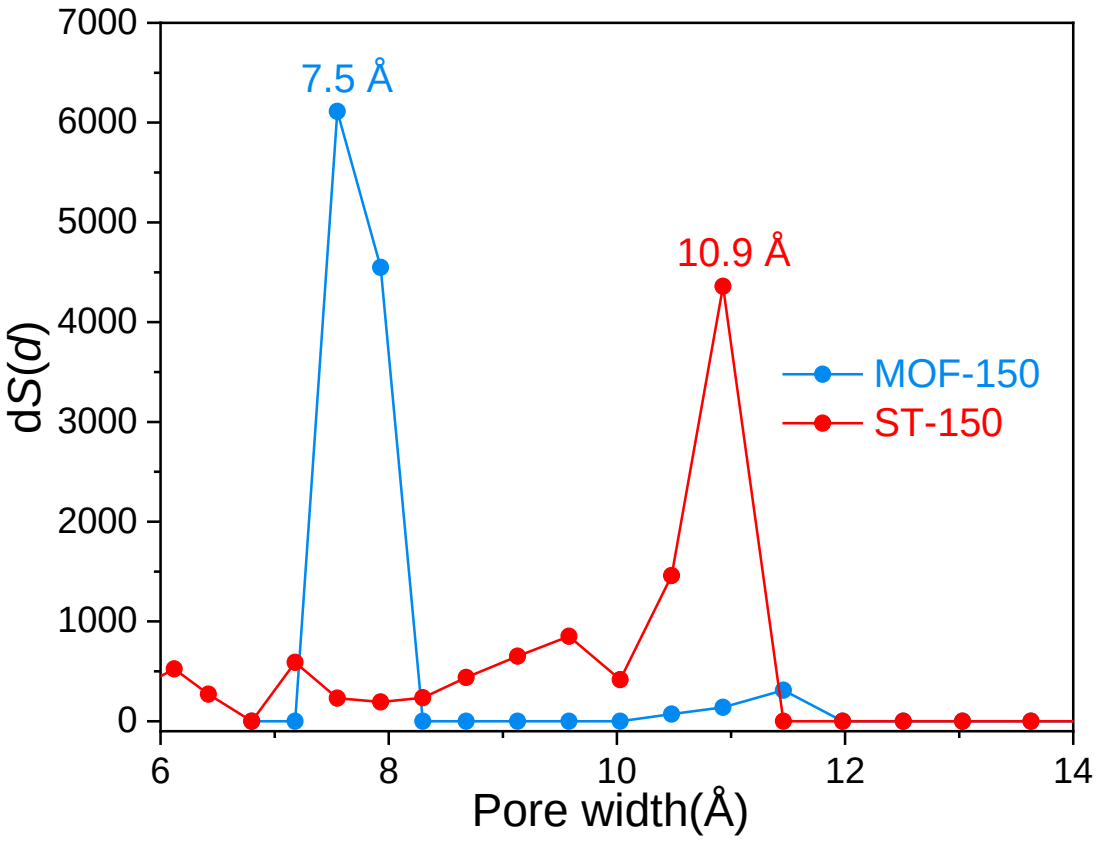

Figure S16. The pore size distribution of ST-150 and MOF-150 derived from the NLDFT/Monte-Carlo model by fitting of the adsorption branch of their Ar physisorption isotherms at 87 K.

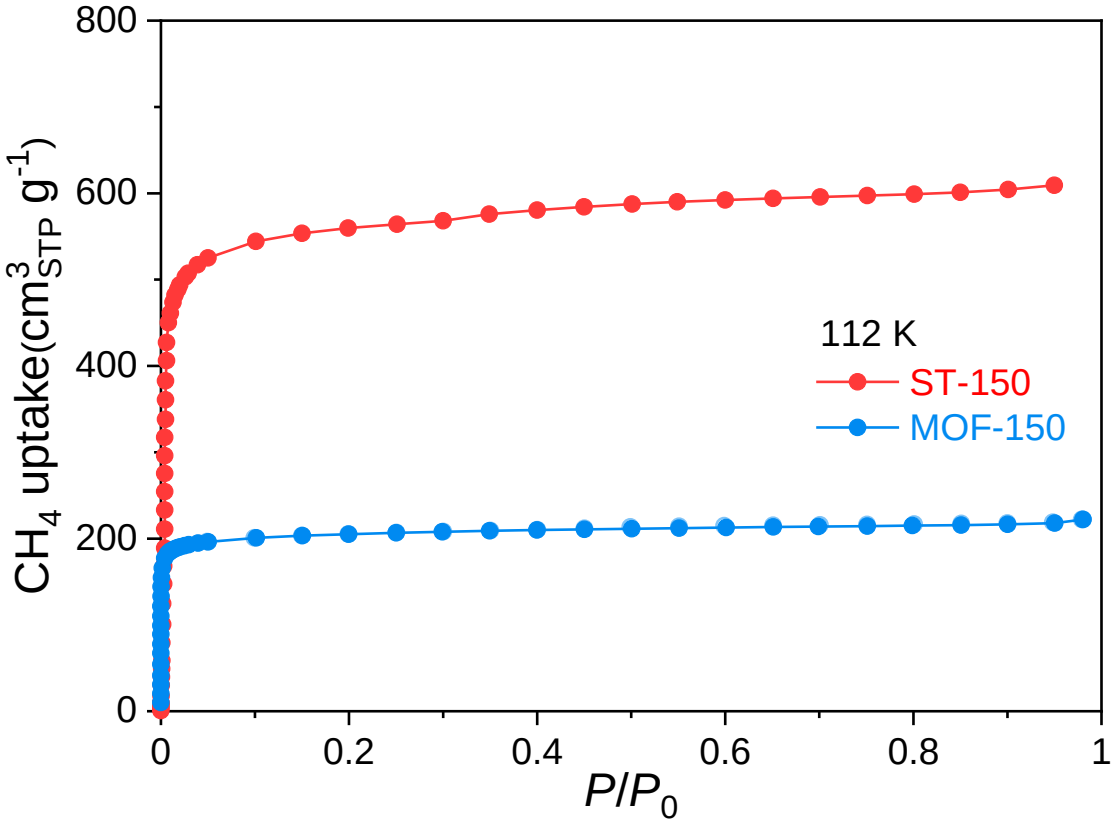

Figure **S17.** CH_4 physisorption isotherms at 112 K for ST-150 and MOF-150 prepared in this work.

Section S4. Methane Adsorption Measurements

High-pressure adsorption isotherms of 200 bar were measured on an iSorb^{TM}HP1 instruments from Quantachrome. About 0.4-0.7 g of activated samples were transferred into a 4.2 mL stainless steel sample holder inside a glove box under Ar atmosphere. The sample holder was then transferred to the iSorb^{TM}HP1, connected to the instrument's analysis station via a VCR fitting, and evacuated at 100 °C for 5 h. The sample holder was placed inside a stainless-steel recirculating Dewar with Ethylene glycol aqueous solution (1:3, *v*/*v*), for which the temperature stability is ± 0.02 °C. The enclosure temperature was set as 45 °C to get rid of the fluctuations of room temperature. Helium is used to determine the void volume at 1, 3, 4, and 5 bar respectively. The iSorb^{TM}HP1 is equipped with two pressure transducers: 1) a 1 bar transducer (accuracy of ±0.01% of full scale) to measure pressures below atmospheric, and 2) a 200 bar transducer (accuracy of ± 0.05% full scale). The background adsorptions were measured with 0.25 mL (about 0.5 g of samples) at different temperatures under the same conditions and using totally the same parameters as sample measurements. Background correction was performed via the iSorb software.

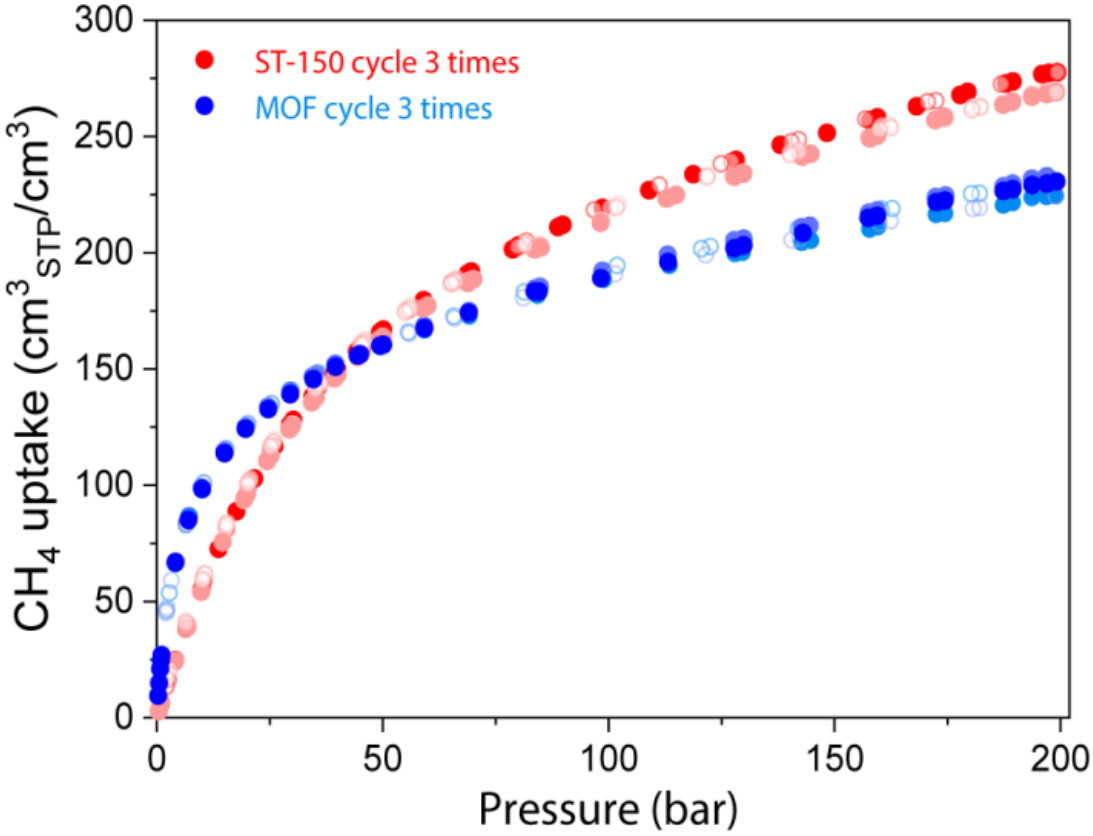

Figure S18. The methane adsorption isotherms (0-200 bar, 298 K) of ST-150 and MOF-150 were measured three times.

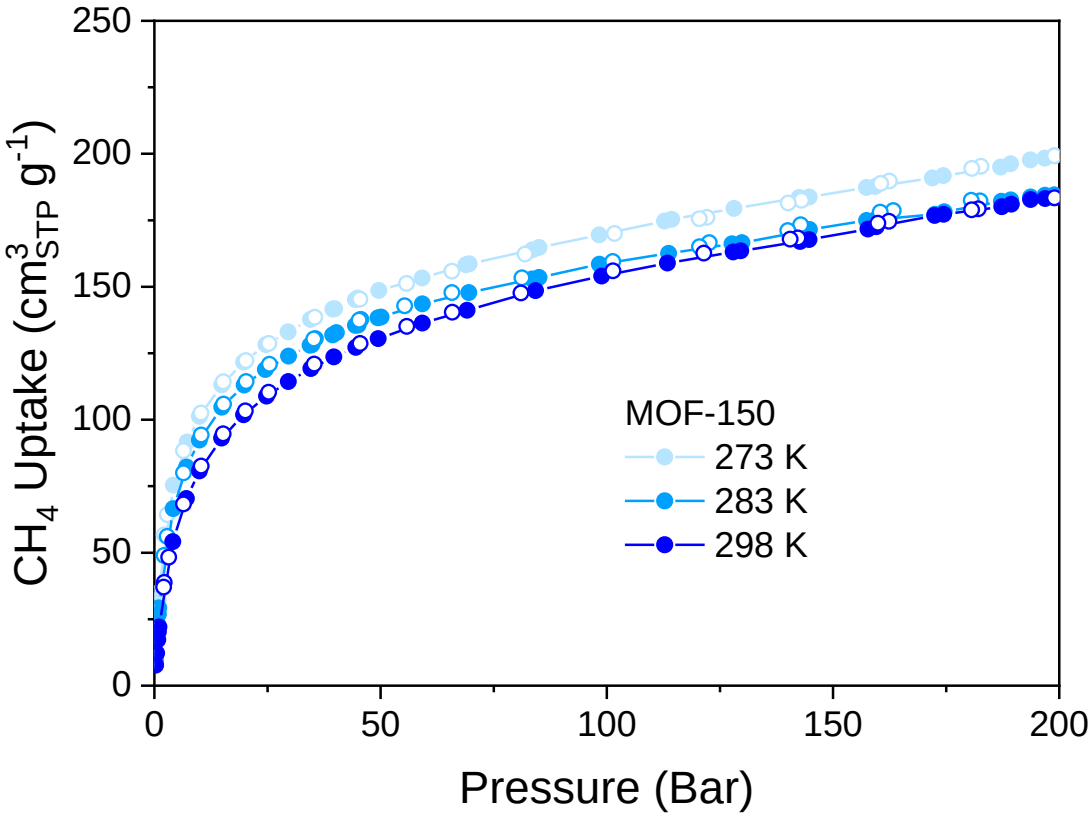

Figure S19. Total CH_4 uptakes for MOF-150 at 273, 283, and 298 K.

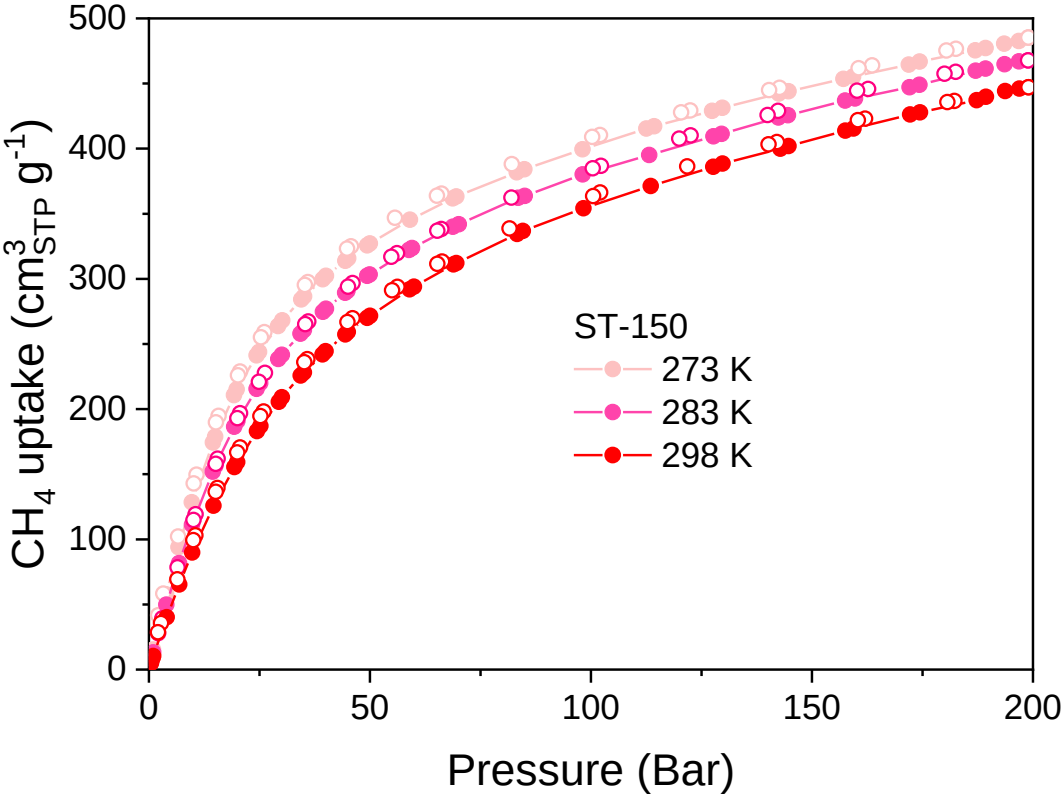

Figure S20. Total CH_4 uptakes for ST-150 at 273, 283, and 298 K.

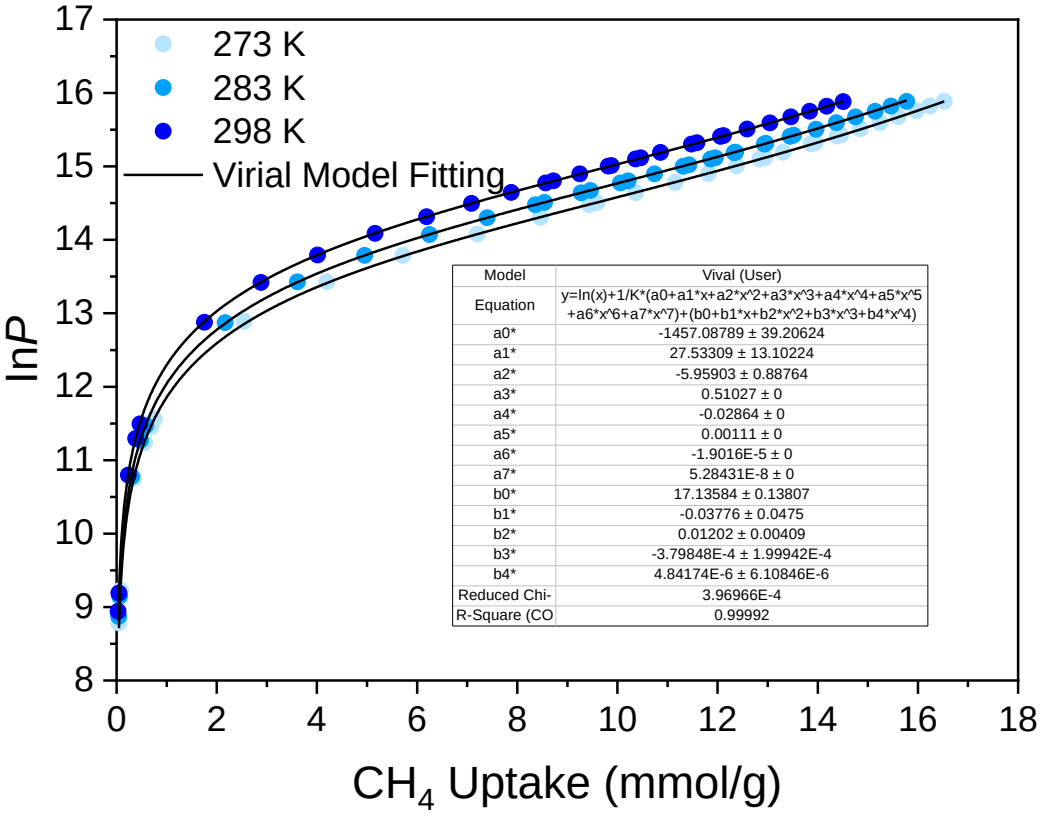

Model	Vival (User)
Equation	y=ln(x)+1/K*(a0+a1*x+a2*x^2+a3*x^3+a4*x^4+a5*x^5 +a6*x^6+a7*x^7)+(b0+b1*x+b2*x^2+b3*x^3+b4*x^4)
a0*	-1457.08789 ± 39.20624
a1*	27.53309 ± 13.10224
a2*	-5.95903 ± 0.88764
a3*	0.51027 ± 0
a4*	-0.02864 ± 0
a5*	0.00111 ± 0
a6*	-1.9016E-5 ± 0
a7*	5.28431E-8 ± 0
b0*	17.13584 ± 0.13807
b1*	-0.03776 ± 0.0475
b2*	0.01202 ± 0.00409
b3*	-3.79848E-4 ± 1.99942E-4
b4*	4.84174E-6 ± 6.10846E-6
Reduced Chi-	3.96966E-4
R-Square (CO	0.99992

Figure S21. Virial Model fitting (lines) of the ST-150 CH_4 adsorption isotherms (points) measured at 273, 283, and 298 K.

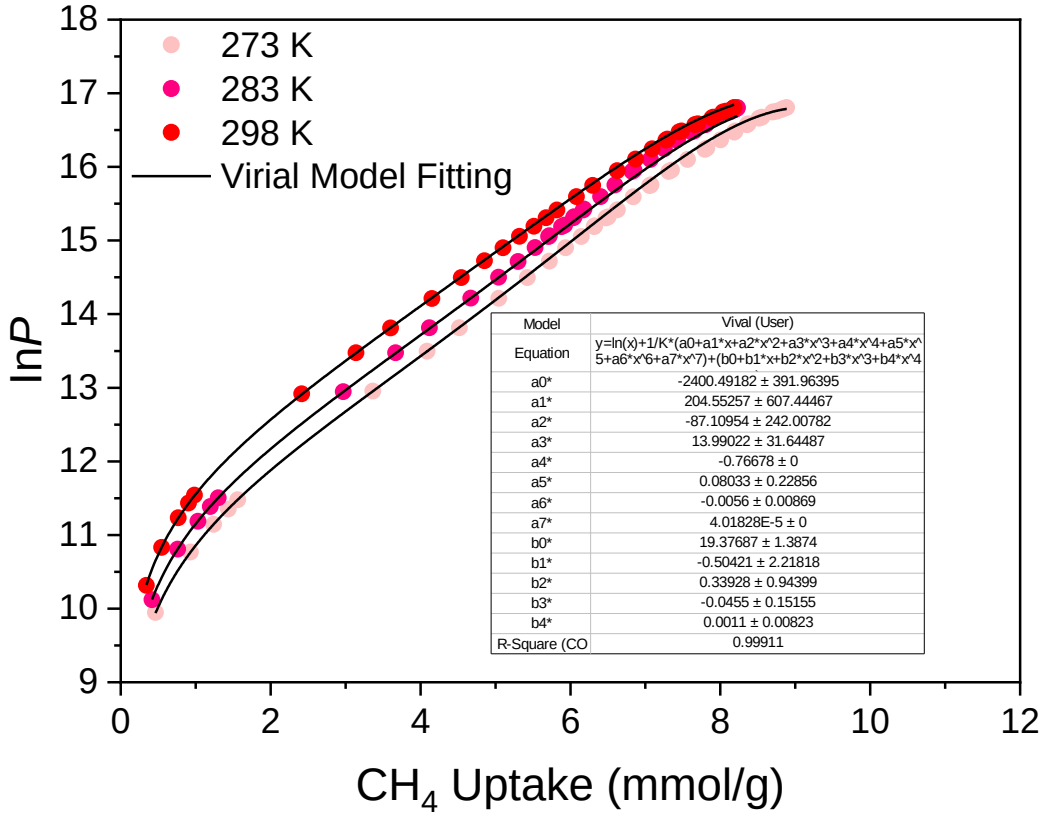

Model	Vival (User)
Equation	y=ln(x)+1/K*(a0+a1*x+a2*x^2+a3*x^3+a4*x^4+a5*x^5+a6*x^6+a7*x^7)+(b0+b1*x+b2*x^2+b3*x^3+b4*x^4
a0*	-2400.49182 ± 391.96395
a1*	204.55257 ± 607.44467
a2*	-87.10954 ± 242.00782
a3*	13.99022 ± 31.64487
a4*	-0.76678 ± 0
a5*	0.08033 ± 0.22856
a6*	-0.0056 ± 0.00869
a7*	4.01828E-5 ± 0
b0*	19.37687 ± 1.3874
b1*	-0.50421 ± 2.21818
b2*	0.33928 ± 0.94399
b3*	-0.0455 ± 0.15155
b4*	0.0011 ± 0.00823
R-Square (CO	0.99911

Figure S22. Virial Model fitting (lines) of the MOF-150 CH_4 adsorption isotherms (points) measured at 273 and 298 K.

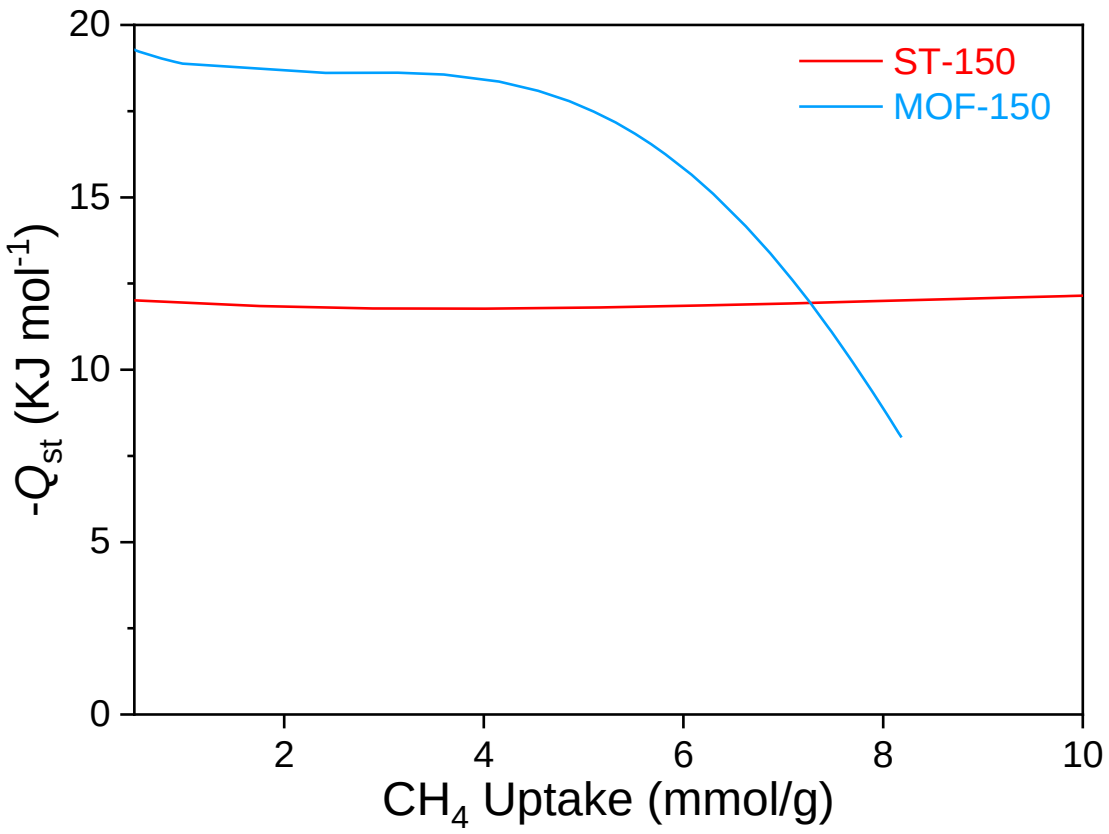

Figure S23. Isosteric adsorption enthalpies of the ST-150 and MOF-150 obtained by using the Clausius–Clapeyron equation using original data fitted by virial model.

Section S5. Solid-State NMR Spectroscopy

Variable temperature (VT) solid-state ^{1}H MAS (Magic Angle Spinning) and ^{1}H→^{13}C CP (Cross Polarization) MAS NMR experiments were performed between −25 and 120 °C on a Bruker Avance III HD 400WB (9.4 T) spectrometer, operating at 400.2 MHz for ^{1}H and 100.6 MHz for ^{13}C, at a spinning speed of 10-20 kHz on a 3.2 mm CPMAS probe. Activated samples were packed into zirconia rotors inside a glove box under nitrogen. ^{1}H spin-lattice relaxation time T_1 was measured using inversion-recovery sequence under nitrogen and also under air. O_2-enhanced CP spectra were acquired under dry air. CP spectra were acquired under dry air with a ^{1}H $\pi/2$ pulse of 2.3 μs, a contact time of 5 ms and a recycle time of 2 s. High-power ^{1}H decoupling was carried out using SPINAL64 with a typical field strength of 75 or 86 kHz. The ^{13}C chemical shifts were referenced externally to glycine COOH at 176.03 ppm. The actual sample temperature was calibrated using ^{207}Pb NMR of solid lead nitrate under the same MAS condition.

Figure S24 and Figure S25 show the VT ^{13}C CPMAS NMR spectra of MOF-5 and ST-150, respectively. For MOF-5 (BDC), the sharp of C3 signal at -8 °C (22 Hz in linewidth at 128.9 ppm) broadened significantly on heating until reaching a maximum of ~ 400 Hz at above 90 °C. In contrast, the linewidths of C1 (COO) and C2 signals (both 7 Hz at -8 °C) increased modestly to 20-40 Hz. This suggests that the phenyl ring re-orientates around the two-fold C1-C1′ axis (so called a π flip) at rates in the order of 1H decoupling frequency. Similarly, in the ST-150 (NTP) NMR spectra the peaks from C3 and C4 broaden with increasing temperature reaching maxima, while C1, C2, and C5 signals increase to much less extent, resulting from the same π flip of phenyl ring.

Using the same approach, we analysed the temperature dependence of the linewidth of phenyl ring CH signals and calculated the activation energy of ST-150 and MOF-150 between 20 and 100 ºC, as listed in Table S5.

Analysis of the C3 exchange dynamics between -25 and 10 ºC, on the other hand, found two exchange systems. The two crystallographically inequivalent linkers likely

differ in steric hindrance against ring rotation, and the crystal chirality result in the two types of linker environments leading to slightly different ring dynamics. ^{13}C CP MAS NMR here is ideal for probing the slow ring dynamics of multiple sites at low temperatures, as such slow motion below 1 kHz and coexisting multiple exchange systems are not readily resolvable by ^{2}H NMR.

On the other hand, the temperature dependence of ^{1}H spin-lattice relaxation time T_1 of ST-150 and MOF-5 were also examined under nitrogen, and there was no correlation with ring motion (Fig. S23), consistent with a previous report by Garcia-Garibay on MOF-5.[13b] The slow ring rotation does not affect ^{1}H T_1, so that it is not applicable for the detection of molecular dynamics with slow rate.

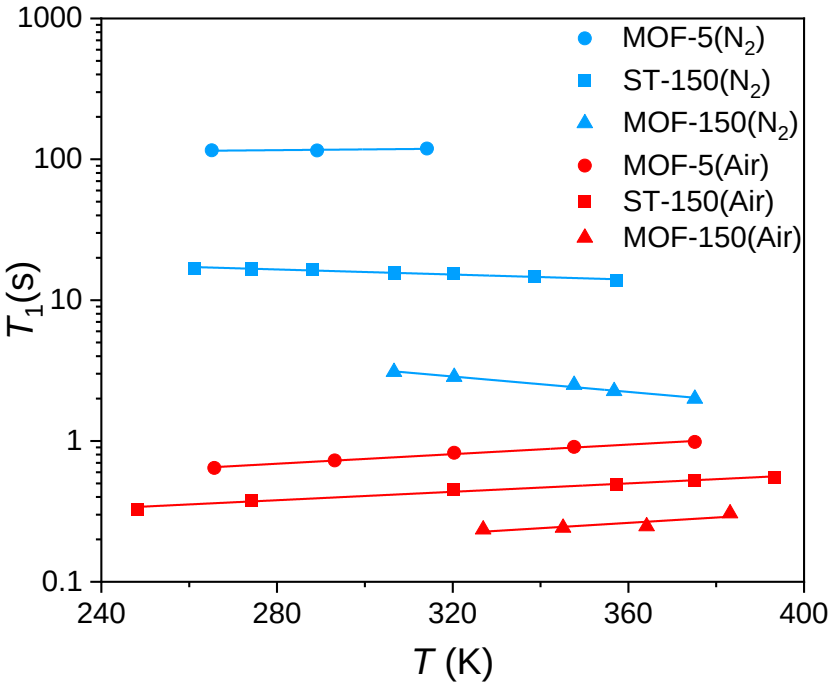

Figure S24. ^{1}H relaxation times T_1 of activated MOF-5 , MOF-150 and ST-150 under nitrogen or air at various temperatures.

Table S5. T_1 of MOF-5, ST-150 and MOF-150 under Nitrogen.

Sample	Atmosphere	Temperature(K)	T_1(s)
MOF-5	Nitrogen	314.15	119.3
		289.15	115.4
		269.15	115.8
ST-150		357.15	13.8
		338.55	14.7
		320.15	15.5
		306.65	15.4
		306.65	15.8
		288.15	16.6
		274.15	16.5
		274.15	16.8
		261.15	16.9
MOF-150		375.15	1.995
		356.75	2.26
		347.65	2.505
		320.35	2.85
		306.65	3.09

Table S5. T_1 of MOF-5, ST-150 and MOF-150 under Dry Air.

Sample	Atmosphere	Temperature(K)	T_1(s)
MOF-5	Air	375.15	0.9834
		347.65	0.9067
		320.35	0.8233
		293.15	0.7267
		265.75	0.6435
ST-150		393.15	0.5491
		375.15	0.5240
		357.15	0.4946
		320.15	0.4563
		274.15	0.3765
		248.15	0.3294
MOF-150		383.15	0.3062
		364.15	0.2479
		345.15	0.2417
		326.95	0.2352
		313.15	0.1457

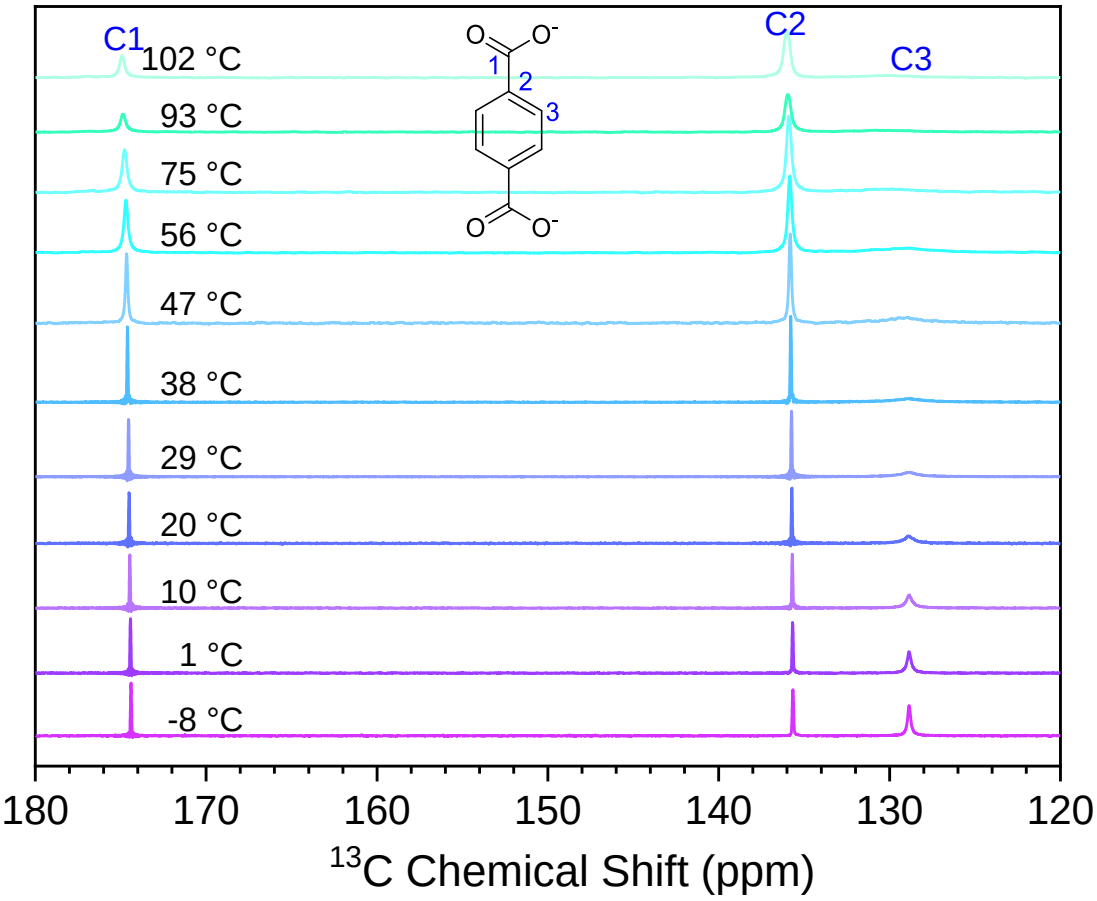

Figure S25. VT ^{13}C CP MAS solid-state NMR spectra of activated MOF-5.

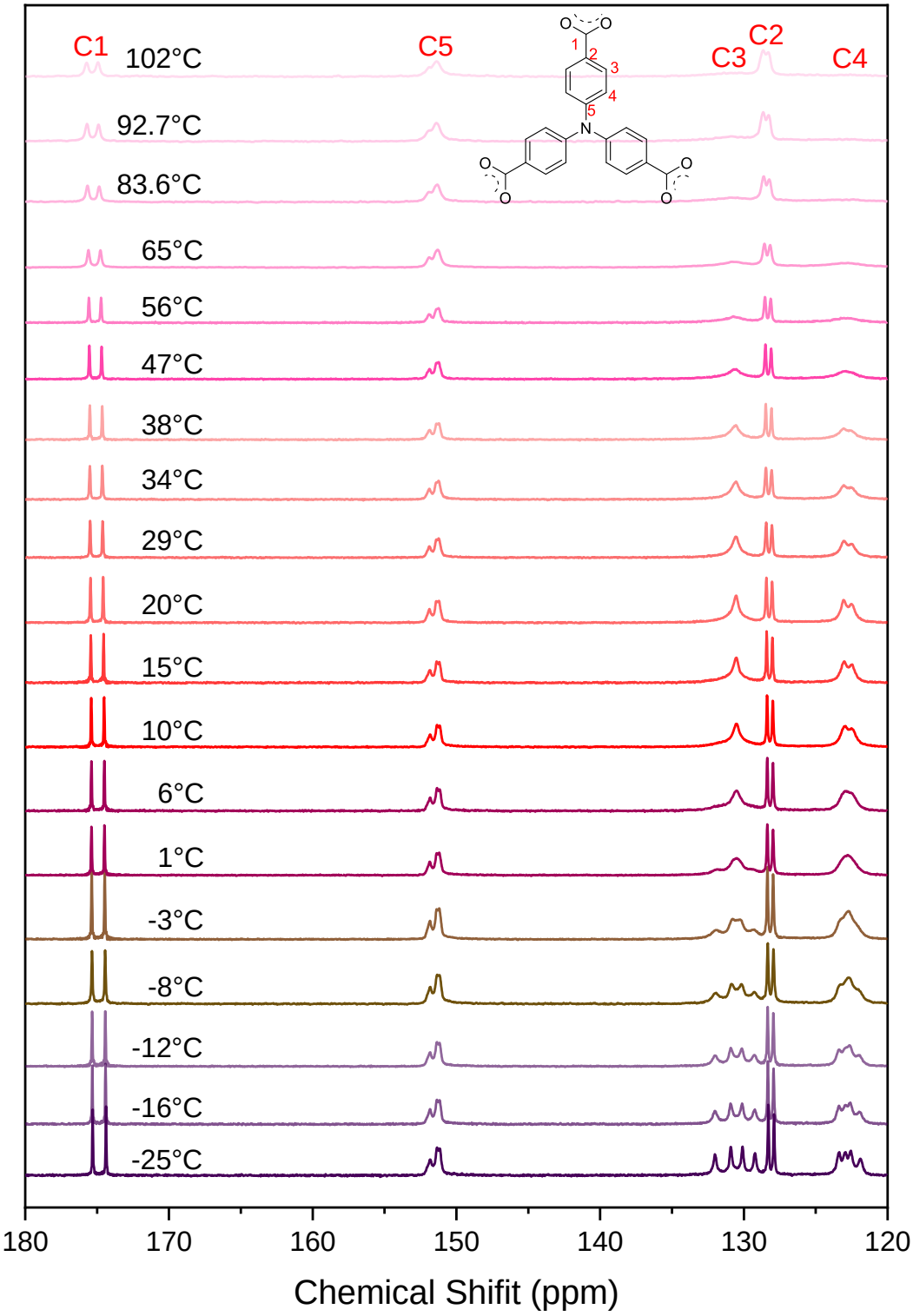

Figure S26. VT ^{13}C CP MAS solid-state NMR spectra of activated ST-150.

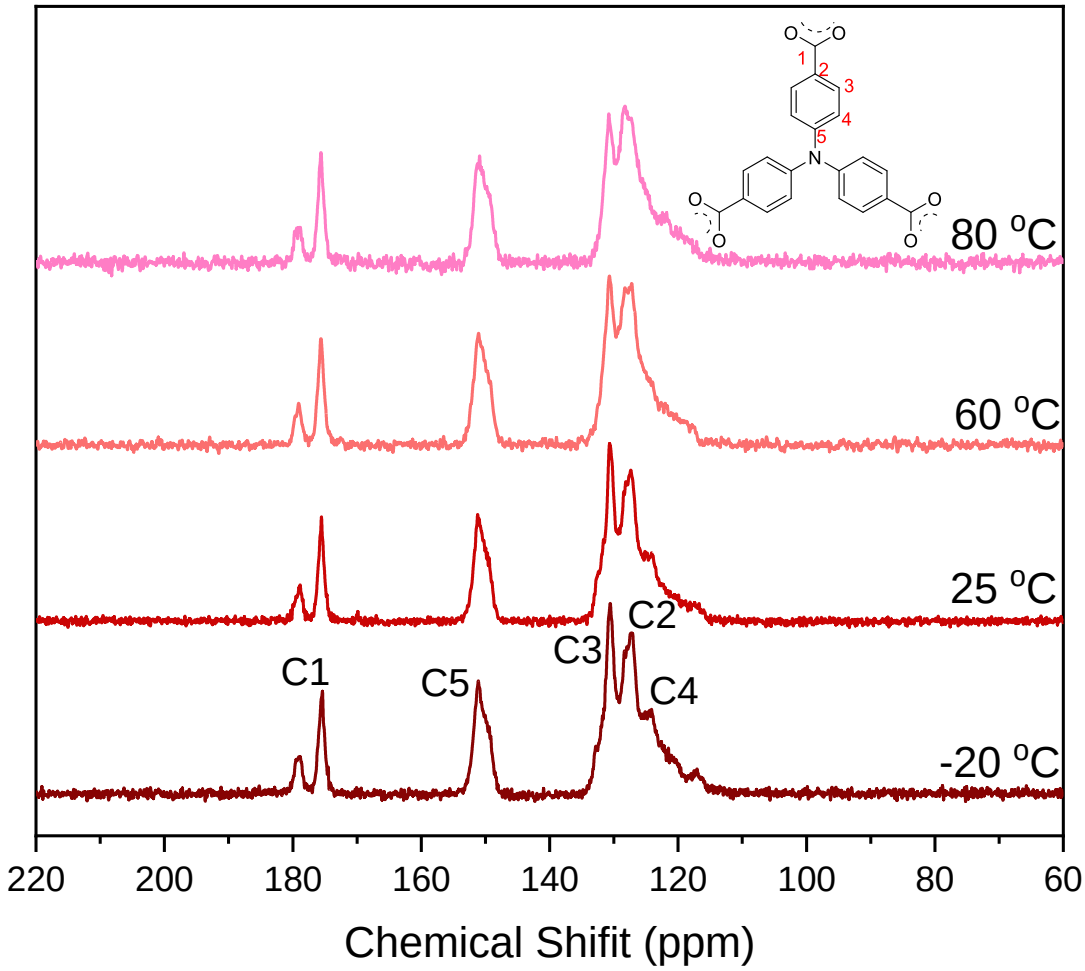

Figure S27. VT ^{13}C CP MAS solid-state NMR spectra of activated MOF-150.

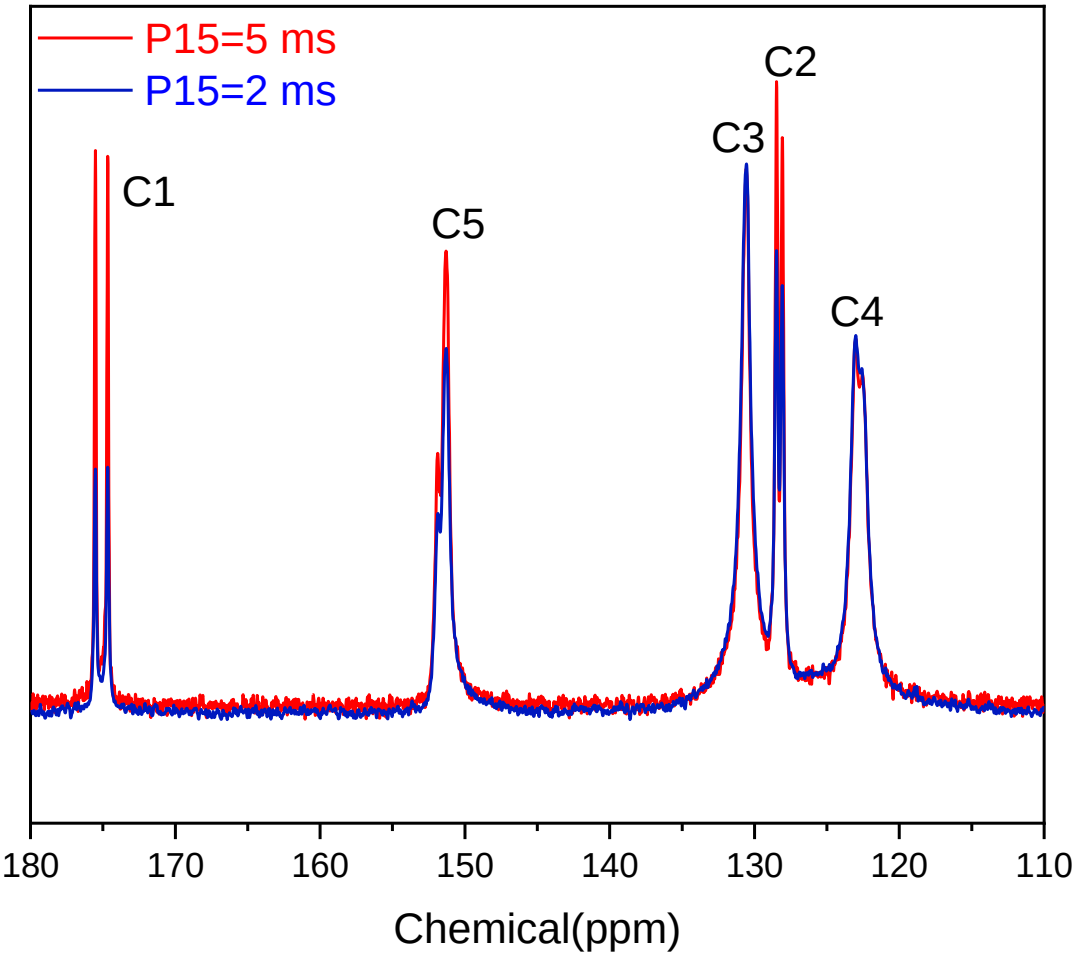

Figure S28. ^{13}C CP MAS solid-state NMR spectra of activated ST-150 by control of CP contact time.

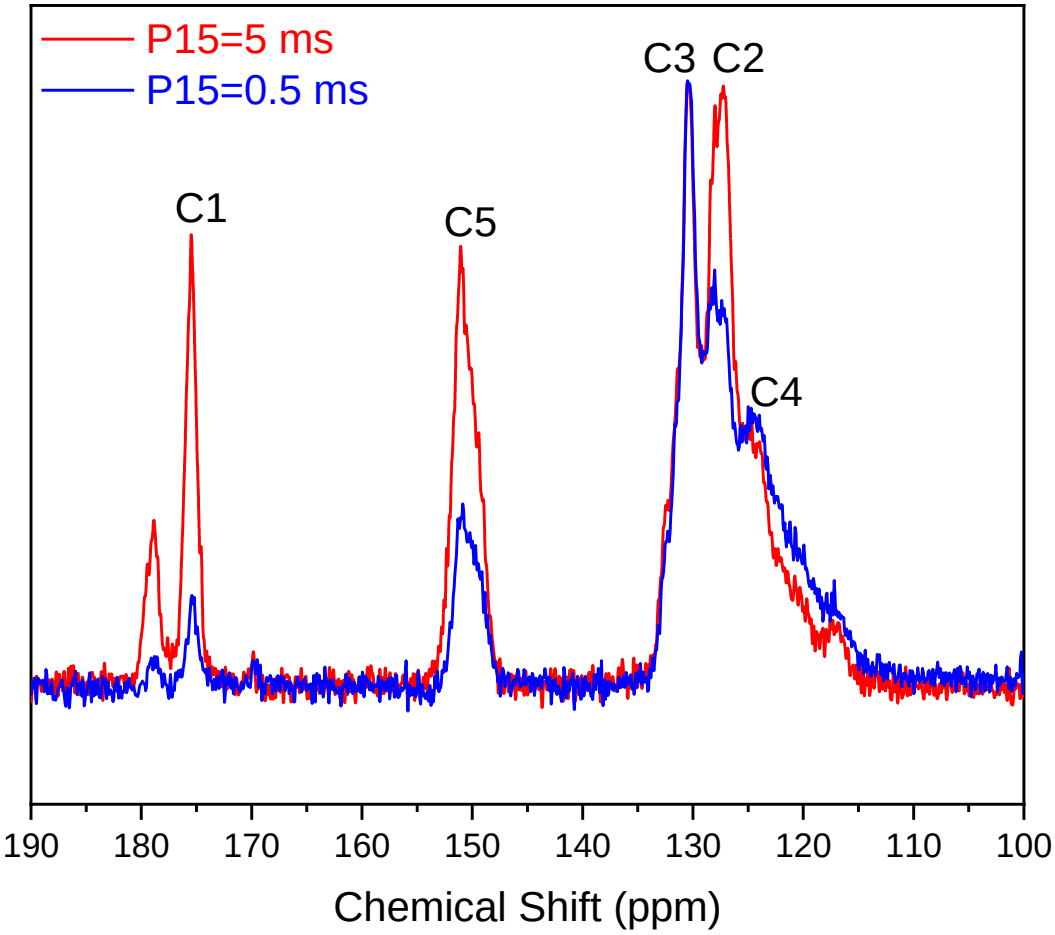

Figure S29. ^{13}C CP MAS solid-state NMR spectra of activated MOF-150 by control of CP contact time.

Table S7. Activation Energy of π-Flip of Phenyl Rings in ST-150 and MOF-5 at Temperature above 20 °C.

	ST-150	MOF-5
Calculation formula	(1) $\ln\triangle\nu = -E_a/RT+K$	(2) $1/T2 = M_2\omega_1^{-1}/2$
	(3) $\tau_0 = \omega_1^{-1}\mathrm{EXP}(-E_a/RT)$	(4) $\triangle\nu = 1/\pi T2$
Slope	3.2025	4.04
ν_1 (Hz)	80000	70000
$\omega_1=2\pi\upsilon_1$	502400	439600
E_a (kJ/mol)	26.6	33.6
M_{2exp}. (rad^2/s^2)	1.2×10^9	1.3×10^9
τ_0 (s)	3.9×10^{-10}	4.8×10^{-11}

Section S6. Molecular Simulation

GCMC Simulation of Methane uptake. The adsorption isotherm of methane at 298K was estimated by performing a grand canonical Monte Carlo (GCMC) simulation implemented in RASPA 2.0. In GCMC simulations, the framework was regarded as rigid. CH_4 was described by the one site united-atom model with the parameters obtained from TraPPE force field. Because a methane molecule is neutral in the TraPPE forcefield, no electrostatic interaction was considered between CH_4 and MOFs. Dispersion interaction energies for MOFs were computed using a Lennard-Jones (LJ) potential form with parameters from the Dreiding force field. The Lorentz−Berthelot mixing rule was used for the pairwise interaction parameters. All pairwise interactions were truncated and shifted to zero at a distance of the cut-off radius of 12 Å. A simulation box was prepared by expanding a MOF unit cell repeatedly to ensure that dimension along each ***x***, ***y***, or ***z*** direction is at least twice the cut off radius. A total of 400000 MC cycles with random translation, rotation, swap, and regrowth (i.e., insertion) moves were used in each simulation; 2×10^5 cycles for equilibrium and the other 2×10^5 cycles for production.

Table S8. Lennard-Jones parameters used in GCMC simulations.

System	Atom type	σ (Å)	ε (K)
MOF	Zn	4.04	27.68
	C	3.47	47.86
	N	3.26	38.95
	O	3.03	48.16
	H	2.85	7.65
CH_4	CH_4	3.73	148.00

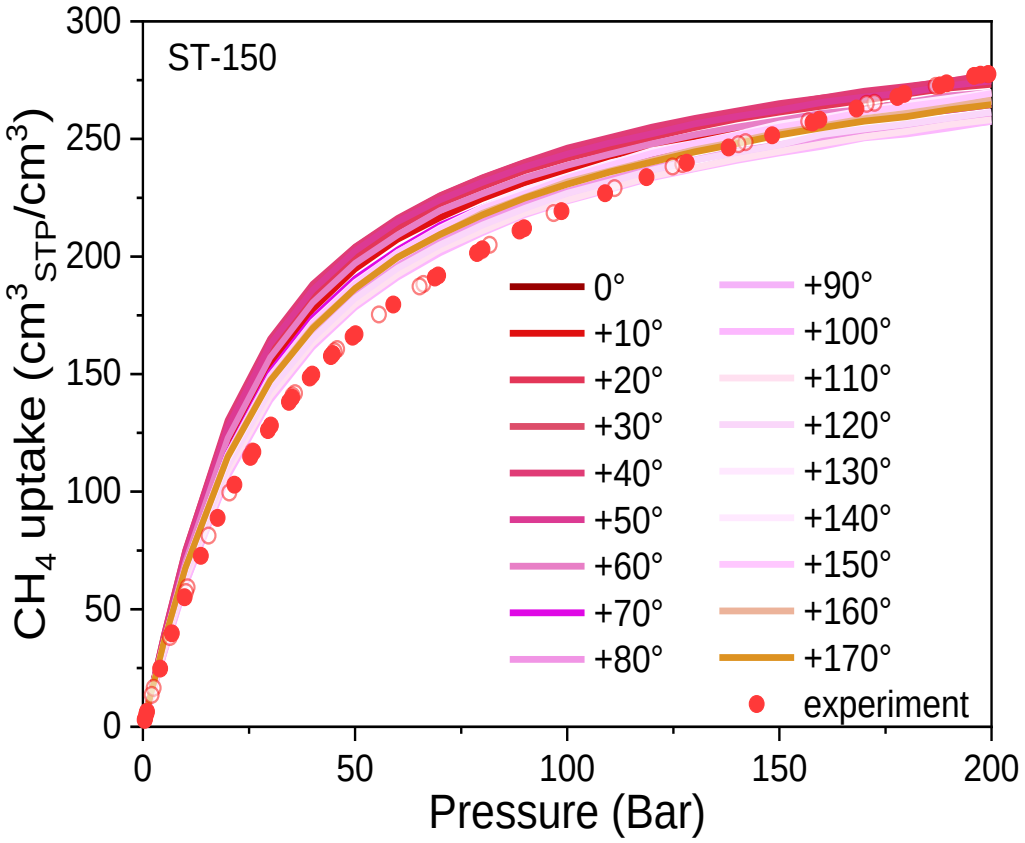

Figure S30. GCMC simulated isotherms of methane in ST-150 in compassion with experimental measurements.

References

S1. Brunauer, S.; Emmett, P. H.; Teller, E. *J. Am. Chem. Soc.* **1938**, *60*, 309.

S2. Sing, K. S. W. In *Adsorption by Powders and Porous Solids*, 2nd ed.; Rouquerol, F., Rouquerol, J., Sing, K. S. W., Llewellyn, P., Maurin, G., Eds.; Academic Press: Oxford, **2014**; p 237.

S3. Thommes, M.; Kaneko, K.; Neimark, A. V.; Olivier, J. P.; Rodriguez-Reinoso, F.; Rouquerol, J.; Sing, K. S. W. *Pure Appl. Chem.* **2015**, *87*, 1051.